

Scaling relations in laser-induced vaporization of thin free-flying liquid metal sheets

H. K. Schubert^{1,2,*}, D. J. Engels^{1,2,*}, R. A. Meijer^{1,2}, B. Liu^{1,2} and O. O. Versolato^{1,2,†}¹Advanced Research Center for Nanolithography, Science Park 106, 1098 XG Amsterdam, The Netherlands²Department of Physics and Astronomy and LaserLab, Vrije Universiteit Amsterdam, De Boelelaan 1081, 1081 HV Amsterdam, The Netherlands

(Received 5 February 2024; accepted 16 April 2024; published 17 May 2024)

We experimentally study the vaporization of free-flying liquid tin sheets when exposed to a 100-ns laser pulse with an intensity between 0.2×10^7 and 4×10^7 W/cm², a case inspired by current developments around “advanced target shaping” in industrial laser-produced plasma sources for extreme ultraviolet (EUV) nanolithography machines. Our findings reveal a gradual vaporization and a linear relationship between the average vaporization rate and laser pulse intensity (with a prefactor of $1.0(3) \times 10^{-7}$ ms⁻¹/W cm⁻²), for various targets ranging from 20 nm to 200 nm in thickness. We introduce a numerical one-dimensional heating and vaporization model based on Hertz-Knudsen evaporation and find excellent agreement between simulations and experimental data. We furthermore demonstrate that the amount of vaporization of liquid tin targets in the investigated laser intensity range is governed solely by the deposited fluence, and collapse all data onto a single nondimensional curve, enabling the accurate prediction of vaporization dynamics in applications in future development of EUV sources.

DOI: [10.1103/PhysRevResearch.6.023182](https://doi.org/10.1103/PhysRevResearch.6.023182)

I. INTRODUCTION

Improvements in semiconductor devices are driven by advances in state-of-the-art nanolithography machines that generate and utilize extreme ultraviolet (EUV) light. This EUV light is produced by the irradiation of mass-limited liquid tin microdroplets with a double laser pulse scheme [1–3]. First, thin liquid tin sheets (“targets”) are produced from droplets using a nanosecond laser prepulse (PP) [4–10]. Picosecond prepulses have also been explored in this context previously [1,3,11]. This first step enhances EUV light generation in a second step where an energetic main pulse (MP) produces a plasma [2,3]. Further efficiency gains in the conversion of MP laser photons into relevant EUV photons in laser-produced plasma (LPP) could potentially be obtained by using advanced target-shaping approaches [2]. Such approaches may include using, e.g., a laser-generated preplasma as suggested in Refs. [12,13].

Inspired by such concepts, Liu *et al.* [14] and Engels *et al.* [15] investigated nanosecond laser vaporization of tin sheet targets with some direct relevance to the industrial use case. More specifically, Liu *et al.* [14] used laser-induced vaporization to uncover previously invisible but important features of the target, such as the center mass and the rim bounding the sheet [10], and proposed scaling relations

(relating, e.g., vaporization times to local sheet thickness) in the underlying dynamics. However, no mechanism was identified and no direct experimental evidence was yet provided in support of the scaling relations. There is a range of literature for metals that are subject to nanosecond laser pulses, where three relevant processes can be identified, namely, (a) boiling, (b) vaporization, and (c) phase explosion [16–19]. Normal boiling (heterogeneous nucleation), perhaps the most intuitive and well-known response of a hot liquid, can be ruled out because of the (microsecond) long time scales involved in the diffusion of vapor bubbles to the surface [17,18], leaving only vaporization (described by the Hertz-Knudsen equation) and phase explosion (also known as explosive boiling or homogeneous nucleation) as viable options. The work of Engels *et al.* [15] focused on spectroscopic analysis of vapor that was laser-produced from tin targets. The vapor was found to have a homogeneous temperature distribution averaging approximately 3000 K and to contain both atomic and nanoparticulate tin. The observation of the rather low-temperature vapor (near the 2875-K boiling point to tin) may fit a gradual Hertz-Knudsen-type vaporization mechanism and could tentatively be interpreted to rule out phase explosion as a mechanism [15]. However, the authors indicated that the presence of nanoparticles could in fact perhaps best be explained by explosive boiling, thus leaving the vaporization mechanism as an open question.

The prior recent works by Liu *et al.* [14] and Engels *et al.* [15] provide a strong basis but leave significant gaps in the understanding of the vaporization dynamics in qualitative (i.e., the vaporization mechanism) and quantitative (i.e., the scaling relations) terms. Addressing these gaps will benefit and steer ongoing developments in improving LPP EUV sources. In this study, we address these gaps in understanding by employing two distinct methods to quantify

*These authors contributed equally to this work.

†versolato@arcnl.nl

TABLE I. Table of targets used in the experiments with columns of their initial droplet diameter D_0 , prepulse energy E_{pp} , initial expansion speed \dot{R}_0 , time in expansion trajectory Δt , nondimensional time $\Delta t/t_c$ (see the main text), and the column for their sheet diameter D_s .

Target	D_0 (μm)	E_{pp} (mJ)	\dot{R}_0 (m/s)	Δt (μs)	$\Delta t/t_c$	D_s (μm)
A	27	56	227	1.2	0.19	396
B _I	27	25	171	2	0.31	382
B _{II}	27	25	171	3	0.46	391
C	35	100	208	1.2	0.13	449

the vaporization process initiated by an auxiliary laser pulse following a PP, for a range of intensities ($0.2 \times 10^7 \text{ W/cm}^2$ to $4 \times 10^7 \text{ W/cm}^2$) and a range of target types and thicknesses (20–200 nm). Our approach involves using a 100-ns auxiliary vaporization pulse (VP) with a temporal and spatial box pulse profile. We image the vaporization during this long pulse stroboscopically using a shadowgraphy technique with 5-ns temporal resolution. The obtained data is employed to demonstrate that the sheet gradually vaporizes (following Hertz-Knudsen evaporation) and to quantitatively study scaling relations to enable predictive modeling of the dynamics.

II. EXPERIMENT

Our experimental setup has previously been described in detail [7,14,20]. Here, we present a summary. In the experiment (Fig. 1) a kilohertz train of liquid tin droplets (temperature 270°C in the experiments) set to a diameter $D_0 \approx 27$ or $35 \mu\text{m}$ is vertically dispensed in a vacuum environment (10^{-7} mbar) by a droplet generator. These droplets pass with a speed of the order of 10 m/s through a horizontal sheet of light that is produced by a continuous-wave HeNe laser and positioned a few millimeters above the center of the vacuum chamber and thus above the laser-droplet interaction point. This light is scattered by the droplets and detected by a photomultiplier tube. Subsequently, the kilohertz signal is down-sampled to 10 Hz and serves as a trigger for the start of the experiment.

Figures 1(a)–1(d) present a schematic of the laser pulse scheme. First, a droplet is hit by the prepulse ($\lambda = 1064 \text{ nm}$, circularly polarized); Fig. 1(a) shows the typical response of the droplet to such PP impact. The PP is generated from a seeded Nd:YAG laser system (Continuum Surelight III) that emits temporally Gaussian intensity pulses with a duration of about 10 ns at full width at half-maximum (FWHM). The PP is focused to a Gaussian spot size of approximately $100 \mu\text{m}$ (FWHM) at the droplet location (at the center of the vacuum chamber). The PP creates a plasma on the droplet, exerting pressure on the remaining liquid tin, which rapidly propels and expands on the order of several 100 m/s to a thin axisymmetric sheet [7,8]. The propulsion, with a velocity U , is oriented along the propagation direction of the laser, while the orthogonal radial expansion starts with an initial velocity \dot{R}_0 at $t = 0$ that is subsequently reduced until it leads to sheet contraction due to the surface tension that is exerted on the edge of the sheet [6,7,21]. The timescales that set both accelerations

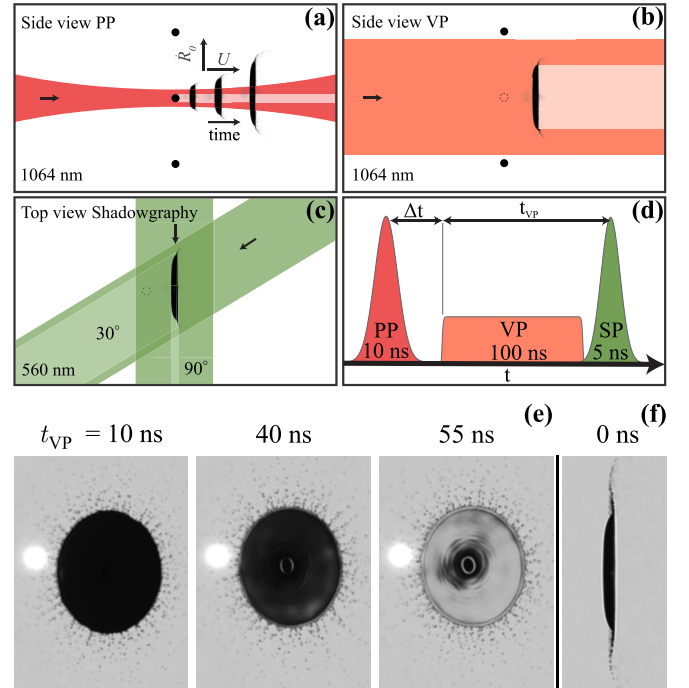


FIG. 1. [(a)–(d)] Illustration of the laser pulse schemes with their irradiation geometries. (a) Side-view schematic of the PP including the tin droplet dynamics of propulsion and expansion resulting from the interaction of PP and the spherical liquid tin drop. (b) Side-view schematic of the VP that irradiates a liquid tin target. (c) Top-view schematic of the shadowgraphy illumination pulses. Arrows indicate the viewing angle. (d) Laser pulse scheme in time, starting with the PP that is followed by the VP after Δt . At time $t = 0$ the PP initiates the droplet deformation process. The time $t_{VP} = 0$ indicates the onset of the VP. The shadowgraphy pulse (SP) is scanned in time over the ongoing VP irradiation of the liquid tin target to capture the vaporization dynamics. (e) A series of front-view green shadowgraphs (at 560 nm) of the thinnest target (B_{II}, see Table I) during irradiation by the VP for different t_{VP} with a VP energy $E_{VP} = 2.5 \text{ mJ}$. The bright spot visible on the left-hand side in the shadowgraphs is due to the PP-induced plasma, the intense radiation of which causes saturation of the charged-coupled device (CCD) chip. (f) Green side-view shadowgraph before irradiation with the VP. PP and VP impact from the left.

are similar to the duration of the laser pulse (nanoseconds) and are much shorter than the timescale of the subsequent fluid dynamic deformation (microseconds) [6,7].

Following Klein *et al.* [22] and Liu *et al.* [9], we obtain the initial radial expansion speed \dot{R}_0 by fitting a linear function through the first three tracked data points of the liquid tin sheet radius, avoiding shadowgraphs with a strong imaging influence of the PP plasma. A higher E_{pp} causes a higher \dot{R}_0 , hence less time is required to obtain a certain sheet size D_s [9].

Inspired by previous work [14], we start our studies on a liquid tin target that provides thickness ranges between 20 nm and 30 nm (according to semiempirical thickness model predictions following Ref. [9] for a 25-mJ PP on a 27- μm -diameter droplet) and refer to it as target B_{II}, consistent with Ref. [14] (for more information about the targets used

TABLE II. Table of input parameters used in the 1D numerical simulation.

Parameter	Value	Source
Refractive index	$3.93 + 7.87j$	Highest T value of Ref. [25]
Conductivity (κ)	43.6 W/(mK)	Highest T value of Ref. [38]
Initial T	800 K	RALEF simulations
Density	6787 kg/m^3	Density at 800 K according to Ref. [39]
Molar mass	0.11871 kg/mol	[31]
Molar heat capacity (c_p)	27.2 J/(mol K)	Value at highest T available [40,41]
Latent heat	$301 \times 10^3 \text{ J/mol}$	[37]
Diffusivity (α)	$28.0 \text{ mm}^2/\text{s}$	Calculated from $\frac{\kappa}{\rho(c_p/M)}$

see Table I). Note that the variation in sheet size is very small, with the relative standard deviation of the B_{II} target size being approximately 1%. We continue our study on a thicker target for the same conditions (i.e., using the same PP and droplet size) but $1 \mu\text{s}$ prior to the target B_{II} , and call it for consistency B_I . This target B_I carries more mass than B_{II} given the continuous mass loss during expansion [9,23]. It also exhibits a stronger thickness gradient along the radial coordinate compared to B_{II} , providing a thickness range between 20 and 50 nm [9]. By increasing the PP energy ($E_{PP} = 56 \text{ mJ}$) we extend our study to a thicker target, achieving a similar D_s but thicker target at even earlier times ($\Delta t = 1.2 \mu\text{s}$). This target is labeled target A [14] with a 50–150-nm thickness range. Lastly, we shoot a significantly stronger PP ($E_{PP} = 100 \text{ mJ}$) at a larger 35- μm -diameter droplet and thus create a target C with an approximate 70–250-nm thickness range [9]. Table I also provides nondimensional times $\Delta t/t_c$ using the capillary time $t_c = \sqrt{(\rho D_0^3)/(6\sigma)}$, which sets the typical time scale for expansion and subsequent retraction, with ρ as input from Table II and $\sigma = 0.54 \text{ N/m}$. The nondimensional apex time for liquid tin droplets is approximately $\Delta t/t_c \sim 0.4$ [21]. This means that only target B_{II} has passed its expansion apex.

In summary, we create different targets to access profiles of different thicknesses (see Table I above, and Fig. 7 in the Appendix for more details), enabling the study of the vaporization dynamics over approximately an order of magnitude in thickness.

We next irradiate these targets with a vaporization pulse with a duration of 100 ns [$\lambda = 1064 \text{ nm}$, circularly polarized, see Fig. 1(b)]. The VP is produced by a laser system with arbitrary subnanosecond pulse-shaping capabilities [24]. The VP laser system generates 100 ns box-shape pulses and is imaged to a spatial top-hat shape at the center of the vacuum chamber with a size of approximately $820 \mu\text{m} \times 820 \mu\text{m}$. We use photodiodes (PDs, DET025AL/M) to monitor the VP before entering the measurement chamber and after transmitting through the chamber. Both laser pulses (PP, VP) are collinearly aligned onto the droplet.

To observe the interaction of the liquid tin sheet with the VP, an imaging setup is used, which is described in detail in Ref. [20]. Briefly, it consists of a dye-based illumination source and CCD cameras that are coupled to long-distance microscopes, yielding a spatial resolution of approximately $5 \mu\text{m}$. The illumination source produces pulses with a duration of 5 ns (FWHM) and a spectral bandwidth of 12 nm (FWHM)

at 560 nm. We use two synchronous shadowgraphy pulses (SP) for backlight illumination of the front- and side-view acquisitions [at 30° and 90° concerning the laser axis, respectively, see Fig. 1(c)] to capture the liquid tin sheet dynamics. Figure 1(d) depicts the time sequence of the aforementioned pulses, highlighting the fact that the SP is scanned (in delay steps) over the ongoing VP ($t_{VP} = 0$ marks the start of the VP); the VP itself impacts at a time Δt after PP. During each delay step, we record 20 frames in a stroboscopic manner, each representing a different laser-droplet interaction event. This allows us to apply postfiltering techniques, e.g., for selecting sufficiently good laser-to-droplet alignment. The excellent reproducibility of the experiment (showcased, e.g., in the small variation in target sheet size) allows the majority of the collected frames to be used for averaging in the following. Figure 1(e) presents front-view shadowgraphs during VP-induced vaporization with $E_{VP} = 2.5 \text{ mJ}$, at various t_{VP} . The shadowgraphs clearly show the presence of the sheet's main features: center mass, bounding rim, ligaments, and fragments [9]. We observe gradual mass removal from the sheet with increasing t_{VP} through the increase in transparency of the sheet to shadowgraphy backlight illumination (see Ref. [14]). Figure 1(f) shows the side-view shadowgraphy of the same target before VP impact at $t_{VP} = 0$.

III. RESULTS

First, we investigate the vaporization dynamics of the thinnest target B_{II} using its partial transparency to the green shadowgraphy backlighting (Sec. III A). We introduce a one-dimensional (1D) vaporization model based on the Hertz-Knudsen equation. Next, we characterize also the thicker targets (Sec. III B). Lastly, we combine and generalize observations of all targets (Sec. III C).

A. Characterization of target B_{II} using partial transparency of the sheet

In Fig. 2(a), a heat map is presented that shows the transmission of background light through the target B_{II} for $E_{VP} = 2.5 \text{ mJ}$. This heat map illustrates the variation in transmissivity as a function of t_{VP} , here taken along a vertical lineout passing through the center of the target [cf. Fig. 2(b)]. These lineouts are aligned and averaged per delay step. The heat map shows that as t_{VP} increases, the target gradually becomes more transparent, indicating a gradual thinning process. The choice

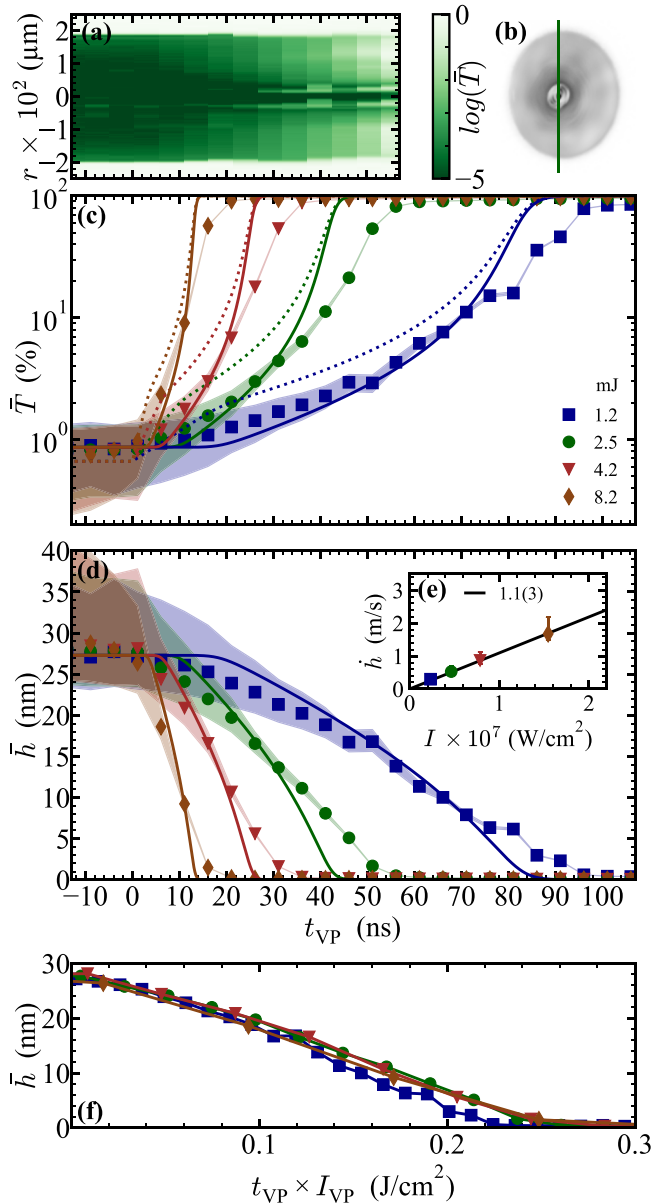


FIG. 2. (a) Heat map of background light transmission constructed from vertical lineouts through the center of the liquid tin target B_{II} from front-view shadowgraphs, as a function of t_{VP} using $E_{VP} = 2.5$ mJ. (b) Front-view shadowgraph with digitally enhanced contrast at $t_{VP} = 36$ ns. (c) Average target transmission values \bar{T} (on a logarithmic scale) during the vaporization of the target B_{II} for energies $E_{VP} = 1.2$ (blue data), 2.5 (green), 4.2 (red), and 8.2 mJ (brown). Shaded areas represent the uncertainty (see the main text). Bold and dashed lines show simulation results using the refractive index with the highest temperature in the literature available (1373.15 K [25]) and an extrapolated refractive index for the expected temperature for each energy case, respectively. (d) Average target thickness values \bar{h} during the vaporization, obtained by applying the transmissivity method to the average transmission values shown in the upper graph. The bold lines show the simulation results. Inset (e) shows average vaporization rates \dot{h} over VP intensity and the result of a linear fit to the data yielding a 1.1(3) proportionality factor. (f) Average target thickness values \bar{h} as a function of deposited fluence.

of a logarithmic scale is motivated by the near-exponential scaling of the absorption of shadowgraphy light with the thickness of the liquid tin target. We note that the central mass feature (see Refs. [9,10]) appears to remain unvaporized. The halo-like, high-transmissivity region observed around the center suggests that the connecting sheet part is particularly thin between the sheet and the central mass feature. Figure 2(b) displays a front-view shadowgraph, shown with artificially enhanced contrast, taken at $t_{VP} = 36$ ns. At this specific time point, the sheet exhibits significant transparency, illustrating the ongoing gradual reduction in thickness.

In Fig. 2(c), we present averaged transmission values as a function of t_{VP} for various E_{VP} . These curves provide a quantitative representation of how transmission values evolve with t_{VP} across the dynamic range of our 12-bit acquisition. To obtain these values, we average transmission values between 100 and 155 μm radius on both sides of the vertically centered sheet lineout. This selected radial range deliberately excludes the center mass and rim features, focusing on regions of this target with approximately uniform thickness (cf. Ref. [9]). The shaded areas surrounding the plotted data points represent the uncertainty range (see discussion below).

We determine the target thickness using a method that utilizes its partial transparency to green backlighting. This approach follows the methods previously outlined by Vernay [26], further developed for liquid tin targets by Liu *et al.* [9]. We employ the TMM [27] PYTHON package to establish a connection between optical target transmission and target thickness. This general transfer-matrix method optics package is used for calculating the reflection, transmission, and absorption of multilayer films. Our more versatile method here slightly deviates from the method outlined in Refs. [9,28], but does not lead to significant numerical differences. We extract, pixel-wise, raw optical target transmission values, denoted by P_{ij} , with i and j representing pixel indices. Before linking the local transmission with thickness, we preprocess the shadowgraphs to account for backlight intensity fluctuations and “dark” value. The parameter P_0 characterizes this overall dark value, including imaging glare sources such as PP plasma, VP scattering, target emission, SP, and electrical noise, all of which contribute to camera exposure. We employ the formula $T_{ij} = (P_{ij} - P_0)/(P_b - P_0)$, with P_b as the mean background value determined from the shadowgraph bin count. To determine P_0 , we average the values of a 9×9 pixel area centered around the center of mass in front-view shadowgraphs, which corresponds to the thickest (and thus darkest) part of the sheet [10]. We separately obtain P_0 values for each VP energy, using frames where the SP arrives before the VP, thus enabling accounting for any potential scattering of the VP onto the imaging system. After establishing the relationship between T_{ij} and thickness h (using the TMM package), we correct for the 30° acquisition angle via $\bar{h} = \bar{h}_{30} \cos(30^\circ)$. In Fig. 2(d), average sheet thickness values, obtained using the data from Fig. 2(c), are presented. The curves demonstrate a continuous decrease in average sheet thickness with increasing t_{VP} . The shaded areas indicate uncertainty ranges resulting from error propagation, dominated by uncertainties in establishing the dark value at 0.046(5), which incorporates a $\pm 10\%$ uncertainty in its determination [this uncertainty also gives rise to the uncertainty region shown in Fig. 2(c)]. We note that

the uncertainty, also in a relative sense, increases sharply with increasing thickness, limiting the application range of the current method to sheet thicknesses below approximately 25 nm. As a consequence, a different quantification method is required for studying thicker sheets. The gradual reduction in sheet thickness over time due to vaporization, as depicted in Fig. 2(d), displays a nearly linear behavior. This motivates us to extract an averaged rate, or a recession *speed*, of vaporization. To calculate the vaporization rates, we determine the time required for the sheet to reduce from its original thickness to approximately 2 nm, using the data from Fig. 2(d).

Figure 2(e) presents the resulting vaporization rates for the various VP intensities. The data reveal a linear dependence of vaporization rate on VP intensity, in line with the claims of Liu *et al.* [14]. By applying a linear fit to these vaporization rates for all intensities, we determine a proportionality factor $d\dot{h}/dI_{VP}$ of $1.1(3) \times 10^{-7} \text{ ms}^{-1}/\text{W cm}^{-2}$, linking vaporization rate to VP intensity. This scaling factor enables us to predict average vaporization rates for a given VP intensity. The observed linear dependence of vaporization rate on VP intensity motivates plotting the sheet thickness as a function of deposited laser fluence $t_{VP} \times I_{VP}$, as shown in Fig. 2(f). This approach results in the collapse of the full dataset, supporting the linear scaling of vaporization rate with intensity and indicating that the thinning is solely a function of the deposited laser pulse energy.

We next use an energy balance model to explain the apparent linear scaling of vaporization rate with VP intensity. The energy required to vaporize a unit volume of tin is $\rho H/M$ (J/m^3), where ρ is the density, H is the latent heat, and M is the molar mass. This energy will be supplied by the laser, which deposits per unit area a power aI ($\text{J}/\text{m}^2 \text{ s}$), where a is the absorptivity of the metal, and I is the intensity of the laser. Balancing these energy terms out gives a rate (m/s)

$$\dot{h} = \frac{aI}{\rho H/M}. \quad (1)$$

Filling in typical values (see Table II for these values) and assuming 20% absorptivity (typical for ~25-nm-thick tin films according to multilayer optical calculations [27]) gives a predicted dependency of \dot{h} on intensity of $1.2 \times 10^{-7} \text{ ms}^{-1}/\text{W cm}^{-2}$.

Inspired by the close match of the simple energy balance argument with the experimental observation, we create a numerical 1D heat diffusion and vaporization solver to model and gain insight into the vaporization dynamics. The 1D space is divided into individual cells with typical cell lengths of 100 pm. For each cell, the temperature is the key variable. Four steps are performed for each time step in the code.

(1) A surface recession speed (v , also one-sided vaporization rate) is calculated based on Hertz-Knudsen evaporation [29] for the front and back surfaces. For the pressure, the vapor pressure following the Antoine equation is used, resulting in

$$v = \frac{10^{A-[B/(T+C)]} M}{\sqrt{2\pi MRT}} \frac{M}{\rho}, \quad (2)$$

where T is the surface temperature, M the molar mass, and R the gas constant. The parameters A , B , and C are 6.60, 16 867,

and 15.47, respectively [30,31]. A cell is considered vaporized when the surface recession (along the surface normal) has passed through the entire cell size. At that moment, it is removed from the simulation domain and no longer interacts with the remaining liquid via heat diffusion.

(2) Recession of the surface causes a reduction in temperature in the cells where vaporization occurs, which are the first and last active cells. This is due to the latent heat required to transform the liquid atoms into gas, and thus to recess the surface. We can obtain a temperature reduction in the cell by balancing the energy input (heat capacity) and output (vaporization)

$$c_p \Delta x \Delta T = H v \Delta t \rightarrow \Delta T = \frac{H}{c_p \Delta x} v \Delta t, \quad (3)$$

where c_p is the molar heat capacity (with units [$\text{J}/(\text{mol K})$]), Δx the cell size, and ΔT the temperature change, giving the input. The output is given by the latent heat H and the size of the vaporized part, which is given by v , the recession speed, multiplied with Δt , the time step. This temperature reduction (and the recession) is calculated at every time step, not only when the entire cell is vaporized; this makes the temperature reduction and thickness reduction “continuous” (with femtosecond time steps) while the cell deactivation is discrete (a few hundred cells).

(3) The first active cell is heated by the incident laser light. The absorptivity of the laser light is continuously updated based on the current remaining thickness of the tin. The absorptivity is calculated using the TMM [27] PYTHON package. The refractive index used is the highest temperature data available for tin [25]. Thus, an energy balance for the laser heating, where absorbed energy is equated to a change in temperature, can be used to obtain a temperature change of the front cell,

$$aI \Delta t = (c_p/M) \rho \Delta x \Delta T \rightarrow \Delta T = a \frac{I \Delta t}{(c_p/M) \rho \Delta x}. \quad (4)$$

(4) The heat is diffused through the active cells. Fourier’s law is discretized using a forward Euler method, resulting in

$$T_i^{t+1} = T_i^{t-1} + \frac{\alpha \Delta t}{\Delta x^2} (T_{i-1}^t - 2T_i^t + T_{i+1}^t), \quad (5)$$

where i indicates the different cells and α is the thermal diffusivity. The prefactor needs to satisfy $\alpha \Delta t / \Delta x^2 < 0.5$ to ensure stability of the forward Euler method and sets the maximum time step to typically 10 fs for our 100-pm discretization.

The sole inputs of the code are the starting thickness and the laser intensity, after which the model calculates the thickness and temperature of the 1D tin slice over time and saves this in output files. Appendix B includes some detail on the sensitivity of the model to the input parameters, while Table II provides an overview of the input parameters used in the simulation. Within the model, the vaporization time t_{vap} is defined as the moment when only 2 nm of liquid tin is left, just as in the experiment. A \dot{h} consistent with the experimental definitions can also be defined by dividing the initial thickness by the time period t_{vap} . To complete the comparison with the experimental observable, the transmission of the 1D liquid

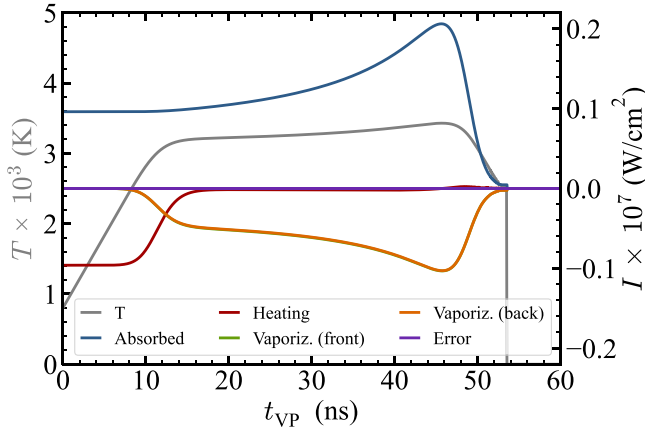


FIG. 3. Example time-resolved output from the 1D numerical code (aligning with the $E_{VP} = 2.5$ mJ case from Fig. 2). The left axis shows the temperature at the laser side over time. The right axis shows the code’s internal energy balance, split in absorbed laser energy, heating of the liquid (which is an energy sink and thus negative, even though the temperature in the liquid goes up), vaporization on the front and back surfaces (which are indistinguishable), and an internal energy “error” being the difference between absorbed energy and the energy loss mechanisms.

slice is calculated using the same TMM package. We also account for the change in the refractive index of tin as it heats and the 30° observation angle of incidence when calculating the transmission via the 1D model.

Figure 3 shows detailed outputs from the code for the $E_{VP} = 2.5$ mJ case in Fig. 2. Initially, the tin is heated rapidly. As the temperature increases, so does the surface recession velocity, as it strongly depends on T . At a certain point, the energy loss to vaporization starts to dominate and even completely stops any heating, perfectly balancing out the input energy by the laser. The final temperature is around the temperature found (approximately 3000 K) in experimentally produced tin vapors [15], underwriting the validity of our approach. We only show the temperature on the laser side since thermal diffusion keeps both sides of the 1D domain at the same temperature within a few Kelvin. This equality aligns with the expectation, given the typical thermal diffusion timescale that can be obtained from Fourier’s law,

$$\Delta t \approx \frac{h^2}{\alpha}, \quad (6)$$

where α is the thermal diffusivity. Taking a conservative value of $\alpha = 16.5$ mm²/s at a low temperature of 505 K [32] and a typical $h = 25$ nm results in a timescale of ~ 40 ps, much shorter than the relevant vaporization dynamics. We also note that the rapid heating induces a refractive index change and thus adds uncertainty to the transmissivity method because this heating cannot be experimentally observed.

The right axis of Fig. 3 also shows an energy balance of the calculations. The energy balance highlights the points mentioned above: an initial heating phase is present before the energy loss to vaporization balances out with the laser input, stabilizing the temperature of the liquid. The absorbed energy peaks when the 1D slice is around 4-nm thick as the absorptivity increases as the sheet thins, increasing

the temperature with it and thus speeding up the surface recession. The absorptivity of the liquid reduces strongly at even lower thicknesses, causing a rapid temperature drop at the end of the vaporization process.

The resulting thicknesses, as a function of t_{VP} , for the different cases are shown in Fig. 2(d). The simulated curves overall show good agreement with the experimental data given the absence of any free-fit parameters. We note that the experimental data points appear to lack the clear plateau that is present in the simulations due to the heating phase. We hypothesize two reasons for this discrepancy. First, the initial temperature of the liquid in the simulation (set to 800 K based on radiation hydrodynamic simulations [33,34]) could be too low, increasing the heating period in the simulation. However, much higher values are not supported by the radiation hydrodynamic simulations. Second, the differences may be due to changes in the refractive index due to heating, causing the experimental method to misinterpret the measured transmissivity. The experimental method cannot distinguish the transmission changing through thinning or heating, and thus will interpret any refractive index change as a thickness change. To investigate the impact of heating on the transmissivity method more, we show two transmission curves (solid and dotted) in Fig. 2(c) that we obtain by applying the (inverse) transmissivity method to the thickness prediction curves from the 1D heat simulation. These curves correspond to two refractive index cases, with the solid line corresponding to the highest temperature for which there is literature data available, $n_{1373.15K} = 3.93 + 7.87j$ [25], and the dotted line using a linear extrapolation of the literature data to the actual temperature (as predicted by the 1D simulations). The results show that the observed transmission falls between the two lines, indicating that the lack of a plateau in the experiment may be due to the changing refractive index—although our linear extrapolation most likely strongly exaggerates the change in refractive index. A second deviation between the simulation and experiment is the lack of increased vaporization rate at very low thicknesses in the experimental data. As mentioned, this accelerated vaporization is a simple consequence of the Fresnel equations, as discussed in detail in Ref. [35]. We speculate that the vapor surrounding the liquid (which absorbs a small amount of light and thus skews the transmissivity measured) obstructs the observation, or that the finite 5-ns length of the illuminating pulse blurs out the effect. Overall, besides these minor differences, we find excellent agreement between simulation and observational experimental data, indicating that the model reliably describes the vaporization process. Our experimental observations, combined with this agreement between simulation and experiment, validate the view of the vaporization process as a gradual process according to Herz-Knudsen, rather than as violent explosive boiling.

B. Characterization of thicker targets A, B_I, and C using edge tracking

After gaining an understanding of the vaporization mechanism for the thinnest sheet in our studies (approximately 25 nm for B_{II}), we now extend our studies to much thicker targets, reaching up to approximately 200 nm in thickness.

For these large thicknesses, the transmission method cannot be used to track the thinning over the full vaporization of the sheet. These thicker sheets are expected to exhibit a larger spatial thickness gradient (see Appendix A, Fig. 7). The presence of such a steep thickness gradient enables us to define and track the edge of the vaporizing sheet, which effectively represents a nearly discrete transition between the fully vaporized and remaining liquid regions. The two regions are characterized by very different contrast levels. This contrast difference is due to the green backlight being able to penetrate through the tin vapor while being extinguished by the remaining liquid sheet part. We refer to the method of tracking the discrete transition as “edge tracking.” We explain the method in detail in Appendix C. This method relies on PD data of the VP exiting the vacuum chamber.

Figure 4(a) displays shadowgraphs of the liquid tin target B_1 , A, and C before VP irradiation in front and side view, allowing a qualitative comparison of the target morphology. Figure 4(b) shows front-view shadowgraphs of the target A for three times t_{VP} for an $E_{VP} = 8.4$ mJ, clearly showcasing the recession of the inner sheet due to vaporization. We observe that the outer and thinner sections of the sheet become transparent earlier than the inner and thicker regions, leaving behind an identifiable inner remaining sheet. This inner radius $R_{inner}(t_{VP})$ is tracked, following the edge-tracking method introduced above. At $t_{VP} = 60$ ns, Fig. 4(b) shows that the rim, ligaments, fragments, and center mass do not fully vaporize. This can be understood from their considerably larger, micrometer-scale thickness [10]. Vaporization of these thick features is only observed when there is a significant increase in VP energy.

Figures 4(c)–4(e) show the edge-tracking results for the inner sheet radii results for targets B_1 , A, and C, respectively. Figure 4(c) shows that the inner sheet radii decrease as t_{VP} increases and that this reduction is sped up at higher VP energies. This observation aligns with our observations shown in Fig. 2 for a much thinner target. The reduction of the inner sheet of the target B_1 [Fig. 4(c)] with time highlights certain differences in target morphology when compared to A and C [Figs. 4(d) and 4(e)]. In the case of target A [Fig. 4(d)], we observe that the rate of reduction of R_{inner} slows down significantly for radii below $50 \mu\text{m}$. This suggests the presence of a thicker center region. The edge-tracking analysis of target C [Fig. 4(e)] reveals even more pronounced differences around the center, with its inner radii converging to approximately $50 \mu\text{m}$, after which the vaporization process seems to end. As shown in the shadowgraph inset, the converging radius is not due to a thicker center region but, rather, a thick rim surrounding a center mass. See Appendix A, Fig. 8, for further detailed shadowgraphs showing this specific feature. The occurrence of such peculiar center mass features is yet not fully understood. In previous work, such features were hypothesized to be attributable to compressible flow effects, specifically to a collapsed cavity generated by the PP [10]. In the current study, we focus on the sheet vaporization dynamics away from any such compressible flow artifacts.

To relate the inner sheet radii to a local thickness, with the final goal of studying the local vaporization rates, we next

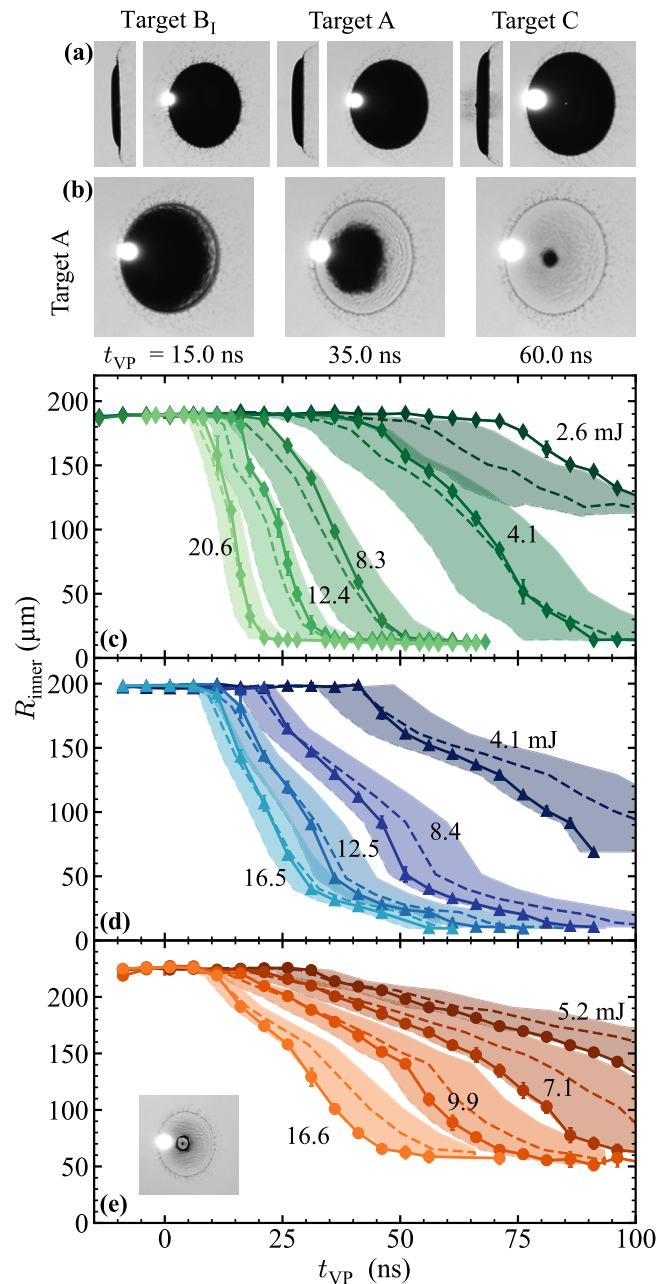


FIG. 4. (a) Side- and front-view shadowgraphs of target B_1 , A, and C before VP irradiation. The bright spots are due to the plasma emission caused by the PP. (b) Front-view shadowgraphs of target A visualizing the vaporization process at times t_{VP} for $E_{VP} = 8.4$ mJ. [(c)–(e)] Inner sheet radii during vaporization for targets B_1 , A, and C, respectively. The inset numbers indicate the used VP energy and the dashed lines are corresponding simulation results (see the main text).

employ the semiempirical thickness model introduced by Liu *et al.* [9] for laser-shaped tin targets such as ours. This model is based on a self-similar solution derived from the model by Wang *et al.* [36]. It assumes an inviscid radially outward flow in the expanding sheet, neglecting curvature-induced radial pressure gradients and sheet features such as the center mass. A solution to the nondimensionalized equation governing the

sheet expansion can be found in the form [36]

$$h^* t^{*2} = f\left(\frac{r^*}{t^*}\right), \quad (7)$$

with the self-similar variables denoted as $r^* = r/D_0$, $t^* = \dot{R}_0 t/D_0$, and $h^* = h/D_0$. Any actual (dimensional) thickness profiles $h(r, t, \dot{R}_0, D_0)$ can be collapsed onto a single self-similar curve $y = f(x)$. Conversely, given any set of experimental inputs (such as droplet radius, time after impact, etc.), the local thickness can be obtained if $f(x)$ is known. Precisely this function was previously obtained by Liu *et al.* [9] as

$$f(x) = \frac{1}{a_0 + a_1 x + a_2 x^2}, \quad (8)$$

with $a_0 = 1.65(2)$, $a_1 = 6.9(3)$, and $a_2 = -2.4(8)$ as parameters that were determined by fitting the proposed $f(x)$ to the available experimental data [9], thus yielding a semiempirical thickness model

$$h(r, t, \dot{R}_0, D_0) = \frac{D_0^3}{a_0 \dot{R}_0^2 t^2 + a_1 \dot{R}_0 t r + a_2 r^2}. \quad (9)$$

Here, \dot{R}_0 is input from the measured initial droplet expansion speed (following Ref. [14], in contrast with the choice of using propulsion U of the original Ref. [9]), D_0 is the initial droplet diameter, and t , r represent time and radial coordinates, respectively. This semiempirical model allows us to effectively characterize the used targets (see Fig. 7 in the Appendix).

Before using this model, we note that target C exhibits a prominent and peculiar inner center rim surrounding the center mass. This feature along with a center mass is not predicted by the model. Consequently, we may expect that the mass that is assumed to be available to produce the sheet is overestimated. We first seek to correct target C for the additional mass loss channels. According to findings from Ref. [10], between 5 and 20 % of the mass is concentrated in a center mass remnant, with no obvious predictive scaling available. Given that we observe both a prominent center mass and an additional ring-like feature, we conservatively take the upper limit (20 %) as an estimate for the mass lost to such compressible flow features. Furthermore, given the large PP energy, we also should correct for the amount of mass that is lost through the ablation process that sets in motion the dynamics. From prior simulations in Ref. [10], and the heuristic scaling law provided therein, we may estimate such ablation losses to account for an additional 20 % mass loss. Thus, in the following, we take target C to have approximately 40 % less mass available on the sheet as would be expected from the initial large droplet size (cf. Fig. 7 in Appendix A).

Next, we return to the vaporization model of Sec. III A. The model requires as input h , here obtained from the semiempirical thickness model, which enables converting the measured R_{inner} (cf. Fig. 4) to a local thickness h . Taking this local thickness h for each R_{inner} as input, the simulation results in a t_{vap} , which is plotted in Figs. 4(c)–4(e) as the dotted curves. The colored bands depict uncertainty estimates based on a 15% uncertainty on the actual thickness. Overall, good agreement is found between simulations and experimental

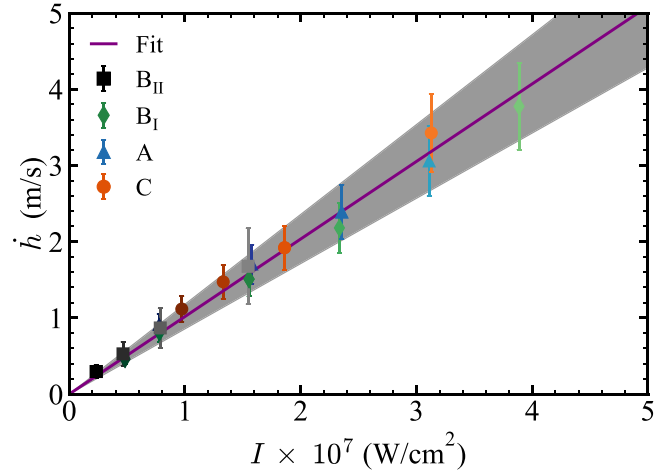


FIG. 5. Average vaporization rates of the targets B_{II}, B_I, A, and C as a function of VP intensity. The purple line shows the result of a linear fit to the concatenated data. The shaded area indicates the fit uncertainty.

data, well within the uncertainty estimates. The agreement is most striking for target B_I aside from the lowest-energy case (2.6 mJ). This minor discrepancy may in part be attributed to uncertainty in the energy calibration. Target A also shows good agreement, but a systematic offset toward later t_{VP} can be tentatively identified. Such an offset may be attributed to the fact that mass is also lost on target A, given that ablation and compressible flow also feature here, if less strongly than for target C. Target C shows the same systematic offset toward later t_{VP} , which may indicate that the applied compressible flow (or ablation) correction still underestimates the true value. Still, there is full agreement between simulation and experimental data within the stated uncertainty estimates over both approximately an order of magnitude in thickness and vaporization laser intensity.

To enable the accurate prediction of vaporization dynamics given a certain laser intensity, we next turn to averaged vaporization rates—reducing the data in Fig. 4 effectively to a single key parameter, \dot{h} . This parameter is obtained by minimizing the difference between (h, r) and $(\dot{h}t_{\text{VP}}, r)$ curves with \dot{h} a free fit factor, a method that is inspired by the approach of Liu *et al.* [14]. We perform the fit in the region of the sheet, well away from the rim and center mass features. The (h, r) values are obtained from Eq. (9) at R_{inner} at $t = \Delta t$ [cf. Table I].

Figure 5 depicts a linear correlation between the thus obtained vaporization rates (\dot{h}) and VP intensity for all targets within the investigated vaporization laser intensity range of approximately 1 W/cm^2 to $4 \times 10^7 \text{ W/cm}^2$.

The rate values for target B_{II} are directly taken from Fig. 2(e). For all other targets (B_I, A, C), the vaporization rates (\dot{h}) are the result of the comparison between t_{VP} and the thickness prediction obtained from the semiempirical thickness model as explained above (cf. Fig. 7). For target B_{II}, the uncertainty arising from the initial target thickness was taken into consideration with $\pm 15\%$ (from the dark value correction), and for all other targets (B_I, A, C), a standard deviation of $\pm 15\%$ was assumed as an uncertainty measure (dominated by the uncertainty in available mass). The observed increase in

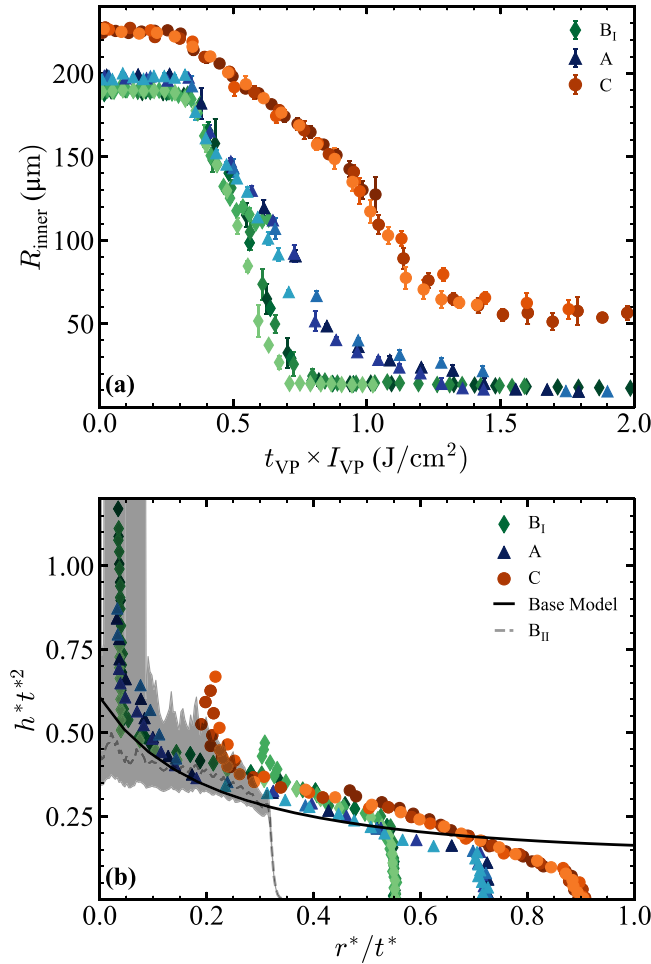


FIG. 6. (a) “Collapse” of the edge-tracking data for R_{inner} for targets B_I , A, and C [cf. Figs. 4(c)–4(e)] when plotted as a function of fluence $t_{\text{VP}} \times I_{\text{VP}}$. (b) Global collapse of the edge-tracking data (targets B_I , A, and C) and B_{II} data (gray data; includes an uncertainty band) in dimensionless units (see the main text). The solid black line indicates the semiempirical thickness model of Ref. [9].

uncertainty with the VP intensity (cf. Fig. 5) is a direct result of the constant delay step size when scanning the SP over the VP, for all measurements, leading to fewer steps during the VP for higher intensities. Finally, we perform a linear fit to the merged dataset of average vaporization rates and obtain a $d\dot{h}/dI_{\text{VP}}$ of $1.0(3) \times 10^{-7} \text{ ms}^{-1}/\text{W cm}^{-2}$, in agreement with and extending the linear scaling of Sec. III A over an order of magnitude in both thickness and laser intensity. The vaporization rate is thus observed to linearly scale with intensity, *independently* of both initial and instantaneous thickness; the time t_{vap} required to vaporize a sheet of thickness h will scale as $t_{\text{vap}} \propto hI_{\text{VP}}^{-1}$ with the \dot{h} at every instant scaling as $\dot{h} \propto I_{\text{VP}}$.

We note that a previous study [14] reported a vaporization rate of 4.4 m/s for a $\sim 0.7 \text{ J}/\text{cm}^2$ fluence laser pulse, 50 ns in duration (yielding an intensity of approximately $1.4 \times 10^7 \text{ W}/\text{cm}^2$), which is a faster rate than would be expected from our observations. However, the authors of Ref. [14] acknowledge an error in a double correction of the vacuum window transmissivity (upscaling the input I_{VP}). Additionally, we have improved on the edge-tracking

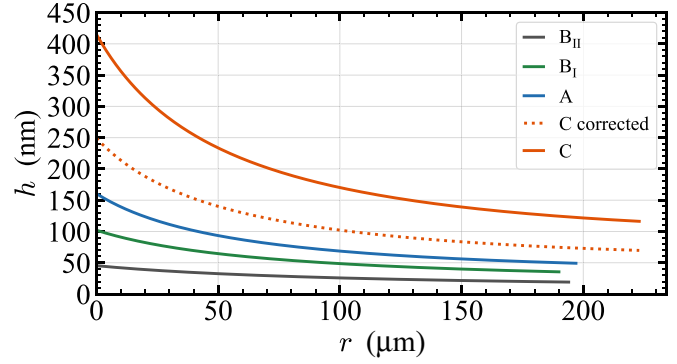


FIG. 7. Thickness profiles according to semiempirical thickness model Eq. (9) for the used targets, with input from Table I in the main text.

method by benchmarking it to the photodiode data, which also causes a slightly different result. Accounting for both differences brings the previous data again in agreement (at $\sim 3 \text{ m/s}$ at $2.2 \times 10^7 \text{ W}/\text{cm}^2$) with the present, more accurate observations.

C. Self-similarities and generalization

We next revisit all experimental data and further study two key findings of this work, namely, that $t_{\text{vap}} \propto hI_{\text{VP}}^{-1}$ and $\dot{h} \propto I_{\text{VP}}$, which can be transformed into each other as $\dot{h} \propto h/t_{\text{vap}} \propto I_{\text{VP}}$. Figure 6(a) shows the result of multiplying the t_{VP} time axis by the VP intensity I_{VP} to arrive at a local fluence $t_{\text{VP}} \times I_{\text{VP}}$ previously presented only as an ansatz in Ref. [14]. It demonstrates that the vaporization of liquid tin targets in the investigated laser intensity range $0.4 \times 10^7 \text{ W}/\text{cm}^2$ to $4 \times 10^7 \text{ W}/\text{cm}^2$ is solely a function of the deposited fluence, across all individual targets. This underpins the first key finding that $t_{\text{vap}} \propto I_{\text{VP}}^{-1}$.

Figure 6(b) presents all experimental data (including that of target B_{II} obtained using the transmission method) in nondimensional units ($h^* t^{*2}$, r^*/t^* ; cf. Sec. III B), with $h = t_{\text{VP}} I_{\text{VP}} d\dot{h}/dI_{\text{VP}}$, taking $d\dot{h}/dI_{\text{VP}} = 1.0(3) \times 10^{-7} \text{ ms}^{-1}/\text{W cm}^{-2}$. All data is found to collapse on a single curve, which underlines the validity of our approach in invoking the self-similar model in Sec. III B and in the mutual agreement of the (transmission vs edge-tracking) methods employed. We may further compare our findings directly with Eq. (9), depicted as a black solid line in the same figure. The edge-tracking curves show reasonable agreement with the self-similar solution that represents a thickness profile, indicating that the edge-tracking data is a good measure to quantify the vaporization process. The collapsed data tend to lie slightly above the self-similar curve, at early times, which may indicate an overall overestimation of the mass available for the sheet (see discussion above). Alternatively, it may point toward a small overestimation of the overall vaporization rate, well within the error bars of Fig. 5. More noticeable deviations occur at the smallest r^*/t^* values, where the experimental data seems to vertically diverge. These deviations are due to the center mass features. Also, at the largest r^*/t^* values deviations appear to occur, but here we note that the self-similar model contains no edge and does not end where

the sheet does. Further deviation at the larger r^*/t^* values may be attributed to finite curvature of the targets, the investigation whereof is left for future work.

IV. CONCLUSIONS

We examine how a liquid tin target vaporizes when exposed to a 100-ns laser pulse (box-shaped in space and time). Our observations are based on stroboscopic acquisitions using an illumination pulse enabling 5-ns time resolution and 5- μm spatial resolution while scanning systematically throughout the 100-ns laser pulse. For thin (~ 25 nm) and flat sheets, the absolute thickness can be obtained from the finite transmission of the backlighting through the sheet, following Liu *et al.* [9]. Our findings reveal gradual vaporization characteristics and a linear relationship between the average vaporization rate with the laser pulse intensity, i.e., $\dot{h} \propto I_{\text{VP}}$. Inspired by the fact that the observed scaling relation may be explained from simple energy balance, we construct a numerical 1D heat and vaporization solver based on the Hertz-Knudsen equation and find excellent agreement between simulations and experimental data. A gradual vaporization mechanism would signal that nanoparticles, as observed in similarly prepared tin vapor targets [15], originate from postvaporization clustering of atomic species. We next extend our investigations to thicker (up to approximately ~ 200 nm) targets, improving on an edge-tracking method previously established by Liu *et al.* [14] in tandem with a semiempirical sheet thickness model [9] to further quantify the vaporization dynamics. Also, here the 1D simulations are in excellent agreement with the experimental data after accounting for additional mass-loss channels. By combining the vaporization rate data from all experiments, we confirm the linearity $\dot{h} \propto I_{\text{VP}}$ with a prefactor of $1.0(3) \times 10^{-7} \text{ ms}^{-1}/\text{W cm}^{-2}$ over the full investigated intensity range ($0.2 \times 10^7 \text{ W/cm}^2$ to $4 \times 10^7 \text{ W/cm}^2$). We furthermore demonstrate that the amount of vaporization of liquid tin targets in the investigated laser intensity range is governed solely by the deposited fluence across all individual targets, and that the time required for vaporization follows $t_{\text{vap}} \propto hI_{\text{VP}}^{-1}$, validating the ansatz proposed in Liu *et al.* [14]. Lastly, we collapse all suitably nondimensionalized data onto the self-similar solution proposed in Ref. [9].

We thus identify the mechanism of laser-induced vaporization (as a gradual vaporization governed by the Hertz-Knudsen equation) at low intensities as may be found in future advanced target preparation schemes for more efficient generation of extreme ultraviolet light. Furthermore, we provide an accurate prediction of the vaporization rates as a function of laser intensity over an order of magnitude around 10^7 W/cm^2 , which is shown to hold for all target thicknesses in a range of approximately 20–200 nm. Our work may guide and find application in the development of future EUV sources.

ACKNOWLEDGMENTS

This work has been carried out at the Advanced Research Center for Nanolithography (ARCNL). ARCNL is a public-private partnership with founding partners UvA, VU, NWO-I, and ASML, and associate partner RUG. This research was funded by the European Research Council (ERC StG 802648).

The authors thank Diko Hemminga for valuable insights into the droplet temperature after prepulse impact, and John Sheil, Michael Purvis, and Haining Wang for valuable discussions. We would also like to thank Henk-Jan Boluijt and Laurens van Buuren for their work on the experimental setup.

APPENDIX A: EXPECTED TARGET THICKNESS PROFILES

Figure 7 depicts thickness profiles of the various tin sheet targets used in the paper, as obtained from the semiempirical thickness model Eq. (9) with the required input taken from Table I in the main text. The dashed line for target C thus shows a mass correction of the target by 40% (see the main text).

Figure 8 displays target C at various stages of vaporization, highlighting an additional feature around its center mass. It shows that this feature is significantly thicker than the sheet and even the rim and center mass, given that it is not vaporized even after the 100-ns-long VP. For more information about the center mass feature in general see Ref. [10].

APPENDIX B: INPUT PARAMETERS IN 1D NUMERICAL CODE

Table II shows the used input parameters for the 1D numerical simulation. The initial liquid temperature of 800 K is estimated from the temperature after the end of the laser pulse in RALEF-2D radiation hydrodynamic simulations such as performed by Poirier *et al.* [34]. A sensitivity study of the model predictions is performed for all input parameters. It is found that t_{vap} is most strongly influenced by the latent heat, which also follows directly out of the energy balance (see the main text). However, the uncertainty on the latent heat is below 0.1% according to literature, so this has a negligible effect on the simulation [37].

The next-strongest sensitivity of t_{vap} is density, and thus also initial temperature, which influences the density. Again, this can be seen in the energy balance in the main text. The uncertainty on ρ itself is only $\sim 1\%$ according to a review of 13 papers [39]. Thus, the initial temperature, and its indirect effect on ρ , gives the largest uncertainty on t_{vap} . We estimate the uncertainty in the initial temperature to be approximately ~ 100 K due to uncertainties in the influence of the prepulse, translating to a 3% effect on the predicted t_{vap} . This uncertainty is significantly smaller than the uncertainty originating from the thickness estimation. Thus, the model predicted t_{vap} may be considered to be rather insensitive to the input parameters. The temperature during the vaporization predicted by the model is even less sensitive to changes in the input parameters. This originates from the exponential dependence on the temperature for the vapor pressure [nominator in Eq. (2)], meaning that only small changes in temperature are required to respond to changes in the input parameters such as ρ or latent heat. Thus, the change in temperature stays below 1%, even for conservatively large (10%) changes in used input parameters.

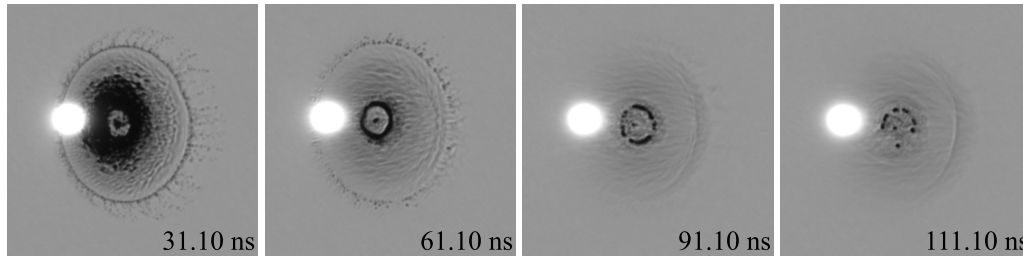


FIG. 8. Shadowgraphs of target C showcasing the observed feature (see the main text) around its center mass at different stages of vaporization.

APPENDIX C: EDGE-TRACKING METHOD

The edge-tracking method relies on PD data of the VP exiting the vacuum chamber. Here, we assume that the geometrical obstruction created by the target, as identified via the 560-nm shadowgraphy, applies directly also to the 1064-nm VP laser light. Separately, we note that neither VP nor SP laser light is absorbed by the vapor (also see Ref. [15]). We establish a correlation between the VP laser light transmitted along the sheet (S , as measured by a PD after the chamber) and our observations of inner sheet radius (R_{inner}), which we extract from the shadowgraphs. This correlation is based on the ansatz that the VP is spatially blocked by the remaining liquid and that the increase of the PD signal S is directly proportional to the decrease in sheet area,

$$[1 - S(t_{\text{VP}})] \propto [R_{\text{inner}}(t_{\text{VP}})]^2. \quad (\text{C1})$$

Note that both quantities (S and R_{inner}) are normalized. Next, to define a sheet edge, a suitable threshold (T) needs to be defined. For this purpose, we perform a Gaussian fit to the background distribution counts, individually for all shadowgraphs, which allows us to determine its mean value (P_{val}) and width (P_{width}). We determine the benchmarked threshold using the relation $T = P_{\text{val}} - B_{\text{level}} P_{\text{width}}$, where we subtract a value $B_{\text{level}} P_{\text{width}}$ from P_{val} that is proportional to the background distribution width with prefactor (B_{level}). This approach enables us to effectively deal with intensity-induced speckle broadening in the illumination. Subsequently, we iteratively adjust the parameter B_{level} and, consequently, the threshold T . With each adjustment, we obtain a threshold-specific inner sheet $R_{\text{inner}}(t_{\text{VP}})$. The optimal value for B_{level} is then found by minimizing the differences between the left- and right-hand side of Eq. (C1). In summary, we obtain a threshold such that the obtained R_{inner} best matches the transmitted VP signal.

-
- [1] H. Mizoguchi, H. Nakarai, T. Abe, K. M. Nowak, Y. Kawasuji, H. Tanaka, Y. Watanabe, T. Hori, T. Kodama, Y. Shiraiishi, T. Yanagida, G. Soumagne, T. Yamada, T. Yamazaki, S. Okazaki, and T. Saitou, Performance of 100-W HVM LPP-EUV source, *Adv. Opt. Technol.* **4**, 297 (2015).
 - [2] I. Fomenkov *et al.*, Light sources for high-volume manufacturing EUV lithography: Technology, performance, and power scaling, *Adv. Opt. Technol.* **6**, 173 (2017).
 - [3] O. O. Versolato, Physics of laser-driven tin plasma sources of EUV radiation for nanolithography, *Plasma Sources Sci. Technol.* **28**, 083001 (2019).
 - [4] D. Hudgins, N. Gambino, B. Rollinger, and R. Abhari, Neutral cluster debris dynamics in droplet-based laser-produced plasma sources, *J. Phys. D* **49**, 185205 (2016).
 - [5] A. L. Klein, W. Bouwhuis, C. W. Visser, H. Lhuissier, C. Sun, J. H. Snoeijer, E. Villermaux, D. Lohse, and H. Gelderblom, Drop shaping by laser-pulse impact, *Phys. Rev. Appl.* **3**, 044018 (2015).
 - [6] H. Gelderblom, H. Lhuissier, A. L. Klein, W. Bouwhuis, D. Lohse, E. Villermaux, and J. H. Snoeijer, Drop deformation by laser-pulse impact, *J. Fluid Mech.* **794**, 676 (2016).
 - [7] D. Kurilovich, A. L. Klein, F. Torretti, A. Lassise, R. Hoekstra, W. Ubachs, H. Gelderblom, and O. O. Versolato, Plasma propulsion of a metallic microdroplet and its deformation upon laser impact, *Phys. Rev. Appl.* **6**, 014018 (2016).
 - [8] D. Kurilovich, M. M. Basko, D. A. Kim, F. Torretti, R. Schupp, J. C. Visschers, J. Scheers, R. Hoekstra, W. Ubachs, and O. O. Versolato, Power-law scaling of plasma pressure on laser-ablated tin microdroplets, *Phys. Plasmas* **25**, 012709 (2018).
 - [9] B. Liu, D. Kurilovich, H. Gelderblom, and O. O. Versolato, Mass loss from a stretching semitransparent sheet of liquid tin, *Phys. Rev. Appl.* **13**, 024035 (2020).
 - [10] B. Liu, R. A. Meijer, W. Li, J. Hernandez-Rueda, H. Gelderblom, and O. O. Versolato, Mass partitioning in fragmenting tin sheets, *Phys. Rev. Appl.* **20**, 014048 (2023).
 - [11] K. Tomita, Y. Pan, A. Sunahara, K. Kouge, H. Mizoguchi, and K. Nishihara, Observation of plasma inflows in laser-produced Sn plasma and their contribution to extreme-ultraviolet light output enhancement, *Sci. Rep.* **13**, 1825 (2023).
 - [12] J. R. Freeman, S. S. Harilal, and A. Hassanein, Enhancements of extreme ultraviolet emission using prepulsed Sn laser-produced plasmas for advanced lithography applications, *J. Appl. Phys.* **110**, 083303 (2011).
 - [13] T. Cummins, C. O’Gorman, P. Dunne, E. Sokell, G. O’Sullivan, and P. Hayden, Colliding laser-produced plasmas as targets for laser-generated extreme ultraviolet sources, *Appl. Phys. Lett.* **105**, 044101 (2014).
 - [14] B. Liu, R. A. Meijer, J. Hernandez-Rueda, D. Kurilovich, Z. Mazzotta, S. Witte, and O. O. Versolato, Laser-induced vaporization of a stretching sheet of liquid tin, *J. Appl. Phys.* **129**, 053302 (2021).
 - [15] D. J. Engels, R. A. Meijer, H. K. Schubert, W. J. van der Zande, W. Ubachs, and O. O. Versolato, High-resolution spectroscopic

- imaging of atoms and nanoparticles in thin film vaporization, *Appl. Phys. Lett.* **123**, 254102 (2023).
- [16] A. Miotello and R. Kelly, Critical assessment of thermal models for laser sputtering at high fluences, *Appl. Phys. Lett.* **67**, 3535 (1995).
- [17] R. Kelly and A. Miotello, Comments on explosive mechanisms of laser sputtering, *Appl. Surf. Sci.* **96-98**, 205 (1996).
- [18] A. Miotello and R. Kelly, Laser-induced phase explosion: New physical problems when a condensed phase approaches the thermodynamic critical temperature, *Appl. Phys. A* **69**, S67 (1999).
- [19] A. H. A. Lutey, An improved model for nanosecond pulsed laser ablation of metals, *J. Appl. Phys.* **114**, 083108 (2013).
- [20] D. Kurilovich, Laser-induced dynamics of liquid tin microdroplets, Ph.D. thesis, Vrije Universiteit Amsterdam, 2019.
- [21] E. Villermaux and B. Bossa, Drop fragmentation on impact, *J. Fluid Mech.* **668**, 412 (2011).
- [22] A. L. Klein, D. Kurilovich, H. Lhuissier, O. O. Versoloto, D. Lohse, E. Villermaux, and H. Gelderblom, Drop fragmentation by laser-pulse impact, *J. Fluid Mech.* **893**, A7 (2020).
- [23] Y. Wang and L. Bourouiba, Non-Galilean Taylor–Culick law governs sheet dynamics in unsteady fragmentation, *J. Fluid Mech.* **969**, A19 (2023).
- [24] R. A. Meijer, A. S. Stodolna, K. S. E. Eikema, and S. Witte, High-energy Nd:YAG laser system with arbitrary subnanosecond pulse shaping capability, *Opt. Lett.* **42**, 2758 (2017).
- [25] G. Cisneros, J. S. Helman, and C. N. J. Wagner, Dielectric function of liquid tin between 250 and 1100 °C, *Phys. Rev. B: Condens. Matter* **25**, 4248 (1982).
- [26] C. Vernay, L. Ramos, and C. Ligoure, Free radially expanding liquid sheet in air: Time- and space-resolved measurement of the thickness field, *J. Fluid Mech.* **764**, 428 (2015).
- [27] S. J. Byrnes, Multilayer optical calculations, [arXiv:1603.02720](https://arxiv.org/abs/1603.02720).
- [28] J. A. Stratton, *Electromagnetic Theory*, 2nd ed. (McGraw-Hill, New York, 1941).
- [29] J. Safarian and T. A. Engh, Vacuum evaporation of pure metals, *Mettalurg. Mater. Trans. A* **44**, 747 (2013).
- [30] D. R. Stull, Vapor pressure of pure substances. Organic and inorganic compounds, *Ind. Eng. Chem.* **39**, 517 (1947).
- [31] National Institute of Standards and Technology, NIST Chemistry WebBook (SRD 69), <https://webbook.nist.gov/> (National Institute of Standards and Technology, Gaithersburg, 2023).
- [32] I. V. Savchenko, S. V. Stankus, and A. Sh. Agadjanov, Measurement of liquid tin heat transfer coefficients within the temperature range of 506–1170 K, *High Temp.* **49**, 506 (2011).
- [33] D. J. Hemminga, L. Poirier, M. M. Basko, R. Hoekstra, W. Ubachs, O. O. Versoloto, and J. Sheil, High-energy ions from Nd:YAG laser ablation of tin microdroplets: Comparison between experiment and a single-fluid hydrodynamic model, *Plasma Sources Sci. Technol.* **30**, 105006 (2021).
- [34] L. Poirier, D. J. Hemminga, A. Lassise, L. Assink, R. Hoekstra, J. Sheil, and O. O. Versoloto, Strongly anisotropic ion emission in the expansion of Nd:YAG-laser-produced plasma, *Phys. Plasmas* **29**, 123102 (2022).
- [35] M. Haddadi, M. B. Das, J. Jeong, S. Kim, and D.-S. Kim, Near-maximum microwave absorption in a thin metal film at the pseudo-free-standing limit, *Sci. Rep.* **12**, 18386 (2022).
- [36] Y. Wang and L. Bourouiba, Drop impact on small surfaces: Thickness and velocity profiles of the expanding sheet in the air, *J. Fluid Mech.* **814**, 510 (2017).
- [37] M. M. Stevanović, Thermodynamic characterization of vaporization of the fourth group elements, *Int. J. Thermophys.* **4**, 353 (1983).
- [38] M. J. Assael, A. Chatzimichailidis, K. D. Antoniadis, W. A. Wakeham, M. L. Huber, and H. Fukuyama, Reference correlations for the thermal conductivity of liquid copper, gallium, indium, iron, lead, nickel and tin, *High Temp. High Press.* **46**, 391 (2017).
- [39] M. Assael, A. Kalyva, K. Antoniadis, R. Banish, I. Egry, J. Wu, E. Kaschnitz, and W. Wakeham, Reference data for the density and viscosity of liquid copper and liquid tin, *J. Phys. Chem. Ref. Data* **39**, 033105 (2010).
- [40] H. Heffan, *Heat Capacity of Liquid Tin* (University of California, Berkeley, 1958), p. 8.
- [41] A. V. Khvan, T. Babkina, A. T. Dinsdale, I. A. Uspenskaya, I. V. Fartushna, A. I. Druzhinina, A. B. Syzdykova, M. P. Belov, and I. A. Abrikosov, Thermodynamic properties of tin: Part I Experimental investigation, ab-initio modelling of α -, β -phase and a thermodynamic description for pure metal in solid and liquid state from 0 K, *Calphad* **65**, 50 (2019).